Seismic wave propagation around subsurface igneous sill complexes

Sanford, O. G. [1*], *Schofield, N.* [2], *Hobbs, R. W.* [1], *Brown, R. J.* [1]

[1] Durham University, Department of Earth Sciences, Durham, DH1 3LE, UK
[2] University of Aberdeen, Department of Geology & Petroleum Geology, Aberdeen, AB24 3UE, UK
*Corresponding author: ogsanford@dunelm.ac.uk

Highlights

- Seismic wave propagation through subsurface igneous sills is studied using full wavefield elastic modelling;
- A representative sill model is developed from seismic and well log data;
- The dominant wavefield factors contributing to degraded imaging are found to be strong internal multiples (stratigraphic filtering), converted modes and leaky guided waves;
- Sub-resolution 'thin' sills have an observable influence on the seismic wavefield.

Abstract

Imaging both within and beneath subsurface igneous sill complexes is a seismic exploration challenge. A significant aspect of this challenge is due to a lack of understanding of the interaction between the heterogeneous geological structures and the seismic wavefield, which includes the seismic response to sub-resolution 'thin' sills. This study aims to provide some insight into the effect subsurface sills have on the observed seismic wavefield. This is achieved

through high-resolution full-waveform elastic seismic modelling, using a realistic geological model developed from interpreted seismic data and statistics of sills from wireline logs and conceptual understanding from sill complexes in outcrop. We find that little energy penetrates through the sill complex to a target reflector below the sill complex, which is consistent with real-world observations. This is due to a number of factors, including energy lost to strong internal multiples (stratigraphic filtering), converted modes and leaky guided waves within the sills. These processes remove energy from the primary transmitted wavefront, contributing to degraded seismic imaging. Whilst these are all fundamental physical limitations that cannot be overcome, further work should focus on the processing of seismic data to ensure that these aspects of the seismic wave-field around sill complexes are optimally treated within processing workflows.

Keywords: seismic; wave propagation; sills; intrusions

1. Introduction

Subsurface intrusive sill complexes consist of a relatively internally homogeneous, high-velocity, high-density sill intrusion within a lower-velocity, lower-density sedimentary host rock. The strong impedance contrast between the sills and the surrounding sedimentary layers contributes to the challenges associated with using seismic reflection techniques to image the structure of such sequences, as is also the case with extrusive basalt sequences (Martini & Bean 2002, Maresh *et al.* 2006, Gallagher & Dromgoole 2007). Hydrocarbon exploration has increasingly focussed on sedimentary basins that contain igneous sill intrusions. Extensive 3D seismic datasets, supplemented by field observations, have helped improve our understanding of subsurface igneous sill complexes, which represent a major form of magma transport within the crust (Smallwood & Maresh 2002, Thomson & Hutton 2004, Archer *et al.* 2005, Cartright and Hansen 2006, Muirhead *et al.* 2012, Wright *et al.*

2012, Schofield *et al.* 2012, Schofield *et al.* 2015, Magee *et al.* 2016, Airoldi *et al.* 2016). Recent research has shown that up to 90% of the sills penetrated by boreholes are 'sub-resolution', where they are below the limits of vertical seismic resolution and are often missed during seismic interpretation (Mark *et al.* 2017, Schofield *et al.* 2015). Furthermore, whilst mafic sills typically have a high velocity and density, due to their Fe- and Mg-rich mineralogy, silicic sills commonly have a lower velocity and density, resulting in a lower impedance contrast with sedimentary rocks and a weaker seismic reflection (Mark *et al.* 2017). During processing, strong internal multiples may contaminate the final migrated image, giving rise to the appearance of sills that are not actually present (Hardy *et al.* 2008), where vertical and sub-vertical igneous dykes are also missed during conventional imaging. A well-known example of poor sill imaging comes from the Rockall Trough, where based upon seismic interpretation, well 164/07-1 was targeting a series of sub-basalt reflections interpreted as interbedded sandstones and shales, however, upon drilling the reflectors were actually found to consist of a series of sill intrusions ranging in thickness from 1.5 m to 152 m that were parallel to the regional stratigraphy (Archer *et al.* 2005).

Sill complexes can have a close association with hydrocarbon sources and reservoirs (Rateau *et al. 2013*), and reliable seismic imaging is critical for the correct interpretation. There have been limited studies into the seismic response of sills based on seismic modelling. 1D convolution modelling using simple planar geometries of sills (Magee *et al.* 2015) can give an indication of the tuning thickness of sills but is of limited use when generating a realistic seismic response. Point spread function convolution modelling can generate data equivalent to pre-stack depth migration (Lecomte *et al.* 2016) and provide a more realistic and computationally fast seismic response to an input model. These studies often use scaled field outcrop models from photogrammetry (Eide *et al.* 2017, Rabbel *et al.* 2018), indicating that sub-resolution

thin sills may be detected on seismic data in the absence of noise. However, these studies are focused on seismic interpretation, rather than the underlying interaction between the seismic wavefield and the complex intrusion network, and neglect the loss of signal throughout a sequence. Hardy et al. (2008) use acoustic full-wavefield seismic modelling and a geologically constrained model of a sill complex to show the challenges of seismic processing around intrusion networks. They show that migration artefacts in the final image, which are caused by internal multiples, may give the appearance of sills that are not present and can result in false interpretations of the subsurface structure.

This study seeks to address the knowledge gap of the underlying interaction between the seismic wavefield and a complex intrusion network. There are three main goals to this study: (1) develop a realistic model of a sill network, using interpreted seismic data, wireline logs and conceptual understanding from sill complexes in outcrop (Section 2a); (2) use full-waveform elastic modelling in a realistic configuration comparable to an active seismic survey (Section 2b); and finally (3) use this model to identify (Section 3) and explain (Section 4) the wave propagation processes, to better understand the interaction of the wavefield with the sills and how this contributes to the reduced sill and sub-sill imaging.

2. Methods

2a. Geological Model

To generate a realistic geological model of a sill complex, both the seismically resolvable 'thick' sills and sub-resolution 'thin' sills must be considered, as the sills imaged on seismic datasets may only represent ~10% of the total intruded volume (Mark *et al.* 2017, Schofield *et al.* 2015). We use an example based on the morphology of an interpreted sill complex from the Paleogene Faroe-Shetland Sill Complex within the Faroe-Shetland basin, in the North Atlantic

(see Figure 11 of Schofield et al. 2015). This is a network of interconnected 'thick' sills, where it is known from well 205/10-2B that large volumes of thin sills are located around the network.

Based upon field evidence of sill networks from the Henry Mountains, Utah (Mark *et al.* 2019), the proportion of thin sills is greatest in the vicinity of large intrusions and reduces away from the thick sill complex. It is not possible to apply sub-resolution 'thin' sills in a deterministic sense (as with the 'thick' sills, which are taken directly from interpreted seismic data), so a stochastic model is developed instead. Other authors use direct field analogues to model the 'thin' sills (Eide *et al.* 2017, Rabbel *et al.* 2018), but the methodology we apply is based on random media theory, which is an effective method to model stochastic heterogeneity within the Earth's crust (Goff *et al.* 1994, Levander *et al.* 1994, Goff & Levander 1996). By combining a large-scale velocity structure (deterministic) and smaller-scale heterogeneities (stochastic), a range of geological scales may be modelled (Larkin *et al.* 1996). Following a similar approach, a random number of 'thin' sills, with variable thicknesses of up to 40 m, are mapped onto the 'thick' sill network that follows the underlying regional stratigraphy and reduce in number away from the sill complex, as observed in the field (Mark *et al.* 2019).

Figure 1 shows the P-wave velocity model. A simple syncline with a compaction gradient (approximately 0.5 s^{-1}) lies under a flat seabed at 500 m depth. This represents the background sedimentary succession but lacks any internal impedance contrasts so that it does not generate any reflectivity that would confuse interpretation of the reflectivity from the igneous intrusions. The deterministic sill complex, taken from a seismic interpretation of a section of the Faroe-Shetland Sill Complex by Schofield et al. (2015), is added to this background model, followed by the stochastic range of thin sills that are morphed to follow the contours of the

background sedimentary model. The P-wave velocity of the sills is set at a single value of 5.75 km s^{-1}, the average sill velocity from well 205/10-2B in the Faroe-Shetland Basin (Mark *et al.* 2017). Below the sill complex is a high impedance sub-sill target reflector (P-wave velocity=6 km s^{-1}), used to test the degradation of the wavefield below sill complexes. Should no wavefield degradation occur within the sill complex, this would produce a perfect reflection within the simulated data. An S-wave velocity and density model are generated based upon an empirical relation with the P-wave velocity derived from Brocher, 2005. No intrinsic attenuation is included within the model, so any signal loss is solely from wave propagation and scattering effects due to the sill complex.

2b. Full Seismic Wavefield Simulations

Full seismic wavefield modelling following a 2-D elastic finite-difference approach is undertaken using *SOFI2D* (Bohlen 2002). The parameters used within the simulations are provided within Table 1. A 2-D model of 4500 by 1000 grid-points is defined, discretised spatially at a 5 m interval, giving a model that is 22.5 km long and 5 km deep. This spatial discretisation limits the thinnest sill that may be modelled to 5 m. However, as Mark et al. (2019) show, the majority of intrusions encountered within wireline logs are greater than 5 m thick. An absorbing perfectly matched layer (PML) boundary of 20 grid points is included on all sides of the model, with no free surface, which eliminates any sea-surface multiples and ghosts and reduces unwanted reflections associated with a finite model domain. Whilst 160 shots were simulated at 100 m intervals, within this paper only two are shown (analysis of the processing into a final migrated section is left for further research). A single shot takes approximately 20 minutes to compute on 50 CPU's (Central Processing Units). A Ricker wavelet with a peak frequency of 14 Hz is used as a point source located at 10 m depth. This represents a typical dominant frequency seen on seismic data at the intruded depths

(approximately 5 km) within the Faroe-Shetland Basin (Schofield *et al.* 2015). This gives a dominant wavelength of approximately 140-280 m in the sedimentary succession, which is significantly longer than the thickness of the stochastically generated sills (that have a minimum thickness of 5 m). A temporal discretisation of 0.1 ms is used to progress the wavefield for 40,000 time steps, to give a total recording length of 4 s. The choice of finite-difference simulation parameters, including the spatial and temporal discretisation, were tested and selected to ensure numerical stability and convergence on an accurate solution (Igel, 2017).

TABLE 1: PARAMETERS USED WITHIN NUMERICAL SIMULATIONS

3. Results

'Snapshots' of modelled seismic wavefield are analysed at discrete time steps for two shot locations, one above the sill complex and one at its edge, to provide a visual understanding of the interaction between the seismic wavefield and the sill complex. One benefit of full wavefield modelling is that the P- and S-wavefield can be viewed separately from the results of the finite-difference simulation (Dougherty & Stephen 1988). Whilst S-wave energy is not created by the acoustic source in the water column, P-wave to S-wave conversion occurs at the boundaries between fluid-solid (e.g. seabed) or solid-solid (e.g. sediment-sill) layers. Converted waves are known to be strongest where there is a high impedance contrast between layers, such as at a sill boundary (Jones 2013).

Figure 2 shows snapshots of seismic wave propagation at four discrete simulation times (0.80, 1.30, 1.80, 2.30 seconds) from a shot located over the thickest section of the sill complex (Shot 1 - Figure 1). After 0.80 s, observing the P-wavefield only (Figure 2a-i), there is a high amplitude P-wave reflection from the top of the sill complex. The first arriving wave within the water column is the direct 'water wave', which is shortly overtaken by the sediment diving wave, which is a refraction through the sedimentary succession generated as a result of the positive velocity gradient. Looking at the S-wavefield (Figure 2b-i), S-wave energy in the subsurface has been generated initially at the seabed, followed by the sill boundaries. This is due to the energy conversion from P-wave into S-wave. By 1.30 s, the P-wave has propagated through the sill complex (Figure 2a-ii). There is high energy loss of the P-wave through the sills, indicated by a low amplitude of the sub-sill transmitted wavefront. This is due to the attenuation of this leading wavefront through the scattering of energy by the high impedance sill complex, due to three causes. Firstly, at the sill boundaries, P-waves convert to S-waves (which will subsequently be referred to as sill converted waves). The high amplitudes of these waves highlight the strong energy loss of the primary wavefront to converted waves (Figure

2b-ii). The strongest amplitude converted waves occur at the uppermost sills in the complex where the point-spreading of the input wavefront is at its least and the primary energy has not been attenuated by further scattering within the complex. Secondly, energy is lost to refractions within the sills. These are leaky guided waves, which result in an almost complete energy loss of the wavefront beyond the critical angle (indicated by the black dashed line in Figure 2a-ii). Leaky waves are characterised by a rapid amplitude loss with distance, compared to the sediment diving wave, for example, which does not exhibit the same energy loss. Finally, strong internal multiples are generated by the wavefield reverberating within the sill complex, which degrades the overall signal and arrives together with the primary reflections from the sills. By 1.80 s, there is a reflection from the sub-sill target reflector, which has a low amplitude due to the lack of energy penetration through the sill complex (Figure 2a-iii). The up-going S-wave energy arising from seabed conversion, which has subsequently reflected from the sill boundaries, and further P-S wave conversions within the sill complex then revert back to P-wave at the seabed and can be recorded on the hydrophones, as the fluid water column is unable to host shear wave energy (Figure 2b-iii). Finally, by 2.30 s, the energy within the water column is dominated by sill converted waves (Figure 2a-iv) having propagated within the subsurface at the slower S-wave velocity. The S-wave energy that has hit the target reflector is very weak and remains trapped and scattered within the subsurface (Figure 2b-iv).

Figure 3 shows snapshots of the seismic wave propagation at the same four discrete simulation times (0.80, 1.30, 1.80, 2.30 seconds) from a shot away from the edge of the thick sill complex (Shot 2 - Figure 1), above several thinner sills. An animation of the P-wave and S-wave propagation corresponding to Figure 3 may be found in the supplementary material. By 0.80 s, primary reflections from the thin sills are visible (Figure 3a-i). These have a significantly lower amplitude than was observed in the simulation with a shot located above the

thicker sills (Figure 2a-i), but in the absence of noise in this simulation, they are still detectable. Rather than forming a discrete reflection from a single sill, they represent a reflection from a combination of thin sills. P-S conversions at the seabed and thin sill boundaries also occur (Figure 3b-i). By 1.30 s, the primary transmitted wavefront has passed through the sill complex to the sub-sill target reflector (Figure 3a-ii). In comparison with Figure 2a-ii, the amplitude of the sub-sill wavefront at the target reflector away from the thick sill complex is stronger than when the wave has passed vertically through the thick sills. Where the sediment diving wave reaches the thicker sills, the wave is either trapped within the lower velocity sediments, in-between the higher velocity sills, or, where the portions of the wavefront reach a sill boundary, it propagates as a leaky guided wave within the sill. Within the sill, eventually the amplitude of this wave reduces to zero, which generates the gaps in the observed wavefront. Similarly, these waves are also converted at the sill, so propagate as guided S-waves (Figure 3b-ii). At this point, the seabed converted energy also reflects from the thin sill boundaries. By 1.80 s, a reflection from the target reflector retains a higher amplitude (Figure 3a-iii) than observed for shot 1 (Figure 2a-iii). There is also a weak P-S conversion from the target reflector below the sill complex (Figure 3b-iii). Finally, by 2.30 s, a high amplitude converted wave from the uppermost thin sills has eventually converted back to a P-wave at the seabed, visible within the water column (Figure 3a-iv). Significant converted energy, mostly from the thin sills, is scattered into the subsurface, and lost (Figure 3b-iv). The transmitted S-wave energy through the sill complex is too attenuated by the time it reaches the sub-sill target so does not provide additional illumination for this target.

The observations from Figures 2 and 3 highlight the main wave types that are generated within the subsurface from a seismic survey above a sill complex. The simulations provide an indication to the level of scattering of energy that occurs, much of which is lost within the

subsurface and not recoverable on data measured during traditional towed hydrophone surveys. Modelled shot gathers for each simulation show the waves that would potentially be observed be observed on a towed hydrophone array. Figure 4 shows the two corresponding shot gathers for a 6 km array, to the left-hand side of each shot. The lack of reflection from the target below the sill complex is clear where the shot is located directly above the thick sill complex (Figure 4a) compared to away from the complex (Figure 4b). Above the thick sill complex (Figure 4a), beyond the uppermost sills, subsequent reflections from each sill are a challenge to identify with the presence of interfering multiple reflections. However, for shot 2 in Figure 4b, reflections from the thin sills are observed. They do not represent distinct reflections from each sill, and are likely a combined reflection response. Strong converted waves from the sills arrive at the hydrophones beyond 2 km offset from the source, which have a higher amplitude than pure P wave arrivals at this offset. For the refractions, leaky guided waves from the sills are not clearly observed on the shot gathers compared to the sediment diving wave. This is due to the rapid loss of energy of the leaky guided wave within the sill complex. These simulated shot gathers highlight that the dominant arrivals that contribute to the measured data are the primary and multiple reflections from the sill complex, and the sill converted waves. The loss of energy throughout the sill complex is clear in the inability to distinguish the target reflection.

4. Discussion

These simulations highlight the fundamental challenges faced during seismic exploration in sedimentary basins containing pervasive igneous sill complexes. This is due to the seismic wavefield effects that are the dominant causes of reduced imaging. The observations made

from the simulations within Section 3 will now be discussed and explained in terms of the dominant causes of reduced sill and sub-sill imaging.

(1) Stratigraphic filtering: the most significant example of reduced imaging is over the thickest portion of the sequence (Figure 2). Thick intrusions may mask deeper intrusions due to stratigraphic filtering effects (Deng 1994). Stratigraphic filtering is the attenuation of a vertically propagating signal through a sequence of thin high and low velocity layers, due to the superposition of primary and multiple reflections. There is a reduction in the amplitude of the transmitted wavefront at each layer boundary. At normal incidence, the high acoustic impedance contrast between the sills and the sediments at the top of the sill complex results in a reflection coefficient of approximately 0.4 (and therefore a transmission coefficient of 0.6) at a single sediment/sill boundary (Figure 4c), corresponding to a 16% reduction of energy at each sill interface through a stack of sills. However, this energy loss is enhanced at each subsequent interface encountered by the wavefront. This also generates a number of multiple reflections generated within the stack of sills. This creates a challenge when processing these data as these may appear to be part of the primary wavefield and they need to be suppressed to enable a robust interpretation. Whilst there are many sophisticated techniques available to remove multiples from seismic data, the fact this multiple energy arrives coincident with the primary reflections and does not have a predictable periodicity makes them difficult to suppress using statistically based deconvolution methods. Therefore, it is likely that some degradation of the seismic image can be expected due to these multiples. This was observed by Hardy et al. (2008), who suggested that internal multiples that have not been sufficiently removed during processing may give the appearance of sills that are not present. However, recent advances in seismic

imaging, such as the Marchenko method which uses multiple energy in generating a seismic image, may be able to take advantage of this (Lomas & Curtis 2019).

(2) Converted waves: for high-impedance contrast media such as sills, the use of elastic modelling as opposed to acoustic is crucial to capture the influence of strong converted modes. These converted modes were missed during the study by Hardy et al. (2008), however elastic simulations are computationally more demanding than acoustic simulations. Figure 5a shows a simple two-layer model of a plane wave arriving at a sediment-sill boundary. At each boundary, a conversion between P and S-wave is likely to occur. Using the Zoeppritz equations (Margrave and Lamoureux, 2019) to calculate the amplitude versus angle behaviour of the wave (Figure 5b), beyond the critical angle (approximately 30 degrees) it is predicted that the reflected converted phases will have a higher amplitude than the P-wave reflection. This study shows that some of the S-wave energy is converted back to P-wave at the seabed, and shows up as high amplitude converted modes on the seismogram. The amplitude behaviour predicted in Figure 5b is therefore observed in Figure 4, where the converted wave is observed after approximately 2 km (which corresponds to a critical angle of approximately 30 degrees) and has a higher amplitude than the sill P-wave reflections at this offset. Otherwise, if it remains as S-wave energy within the subsurface, this represents lost energy from the overall wavefield that contributes to degraded imaging. Converted modes are also subject to the stratigraphic filtering effects as experienced by the primary wavefront. It is often suggested that the converted modes may be used to aid imaging (Jones 2013), however, given the lack of converted mode energy that returns to the surface from the deepest parts of the thick-sill sequence or the target reflector (Figure 2d-ii), the observations from the simulations suggest that it is unlikely to be beneficial for sub-sill imaging.

(3) Leaky guided waves: the propagation of the sub-horizontal refracted energy within each individual sill takes the form of leaky guided waves. They are called this as the energy propagating within the sills leaks out, resulting in an overall reduction in amplitude of this wave with distance propagated along the sill. Waveguiding effects are observed in many situations, such as leaky waves in gas hydrate layers (Zanoth *et al.* 2007), but have not been reported for sill complexes. Given the rapid attenuation of the leaky guided waves, it is unlikely that the use of these would improve imaging, particularly as they are not clearly observed on the shot gathers in Figure 4. As the guided wave does not propagate the length of the sill, it cannot be used to estimate it's horizontal extent. Much of the guided wave energy arrives outside of the direct water wave, therefore most of this would likely be muted during seismic processing, although care must be taken to ensure no guided refracted energy around the critical offset is included within reflection processing workflows. Energy trapped and propagating in-between sills within the sediments as trapped components of the sediment diving wave are unlikely to form an important contribution to the measured wavefield, as this energy may only be returned to the surface at very long offsets and because it propagates at the background velocity as part of the refracted wavefield.

(4) Sub-resolution thin sills: The modelling performed here suggests that in the absence of noise, reflections from thin sills are observable at low frequency (14 Hz). However, as they have a low amplitude, the arrivals are likely to be unobservable in the presence of ambient noise associated with the collection of seismic reflection data. Where multiple thin sills are present then stronger reflections may be created by constructive interference, so a reflection may be wrongly interpreted as a being from a single sill or interfaces in a sedimentary succession, as was the case in 164/07-1 (Archer et al., 2005). It should be noted that there

are less sills present within this simulation than would be present in reality, due to metre and sub-metre scale sills that have been observed in outcrops (Eide et al 2017, Mark et al 2019).

The model presented here may be considered as a starting point for further research to improve understanding of the interaction of seismic energy with sill complexes,. The model can be developed in many ways, such as including an extrusive basalt overburden (as is common in the Faroe-Shetland Basin), creating more interconnectivity between the sills by including feeder dykes, adding metre to sub-metre scale heterogeneity from outcrops, and extension to consider the full 3D geometry of a sill complex. Additionally, ocean bottom nodes may record information, particularly converted waves, that may be missed on hydrophone data. The predicted response on an ocean bottom node may be directly simulated using full-wavefield modelling techniques. Though the results within this study focused on the wave propagation effects, further work should include analysis of the final processed image of all the shots by undertaking full processing of synthetic data and making direct comparisons to real seismic datasets. As part of this processing, it may prove possible to test strategies that could improve the final image that reduces the risk of misinterpretation. This could include performing full-waveform inversion (FWI), which has the potential to resolve fine-scale features such as thin sills, but requires a good starting velocity model (Morgan *et al.* 2013). Another possible development would be to integrate this type of modelling into the workflow where seismic interpretation of sill complexes is used to understand subsurface magma transport from a volcanological and/or hydrocarbon point of view (e.g. Schofield et al. 2015; Jackson *et al.* 2020, Walker et al. 2020, Phillips & Magee 2020).

5. Conclusions

By simulating the entire seismic wavefield around a subsurface sill complex, we have highlighted the dominant causes of reduced sub-sill imaging as strong energy attenuation. This occurs due to internal multiples and stratigraphic filtering, the conversion of P-wave energy to S-wave energy, and refractions within the sills in the form of leaky guided waves. There is almost a complete loss of seismic energy penetrating the sill complex to a sub-sill target reflector. Thin sills are shown to have an influence on the overall wavefield, and are detectable at the frequencies simulated within this study. However, they may fall within the background noise level measured on real seismic reflection data.

These observations have implications for sub-sill imaging, as these are fundamental wave propagation processes which are a challenge to overcome. Further improvements to sub-sill imaging could be achieved through seismic processing, however this warrants continued investigation through the use of simulated datasets, for which the velocity model is known and developed from seismic, well log and field outcrop data. This will provide confidence for the processing schemes applied to real seismic data gathered from above sill complexes, and ensure that these aspects of the seismic wave-field around sill complexes are optimally treated within processing workflows. Where seismic data around sill complexes is used to understand magma transport within the crust, it should be recognised that there are fundamental challenges with imaging sills, which may influence the interpretation of deeper subsurface magma transport. In particular, it is likely that not all sills are imaged from deeper within the complex, or the multiply scattered wavefield has become too complex to be confident about its interpretation.

Acknowledgements

This work was undertaken during O.G.S's PhD at Durham University, funded by Eni through the Volcanic Margins Research Consortium (Phase 2). Seismic modelling was performed using the open source SOFI2D (Bohlen 2002) and post-processed using Seismic Un*x (Stockwell & Cohen 2012). Figures were prepared using the open source Generic Mapping Tools (GMT) (Wessel & Smith W. H. F. 1998) and Seismic Un*x. Zoeppritz amplitude coefficients were calculated using the CREWES Matlab toolbox of the University of Calgary (Margrave and Lamoureux 2019). This work made use of the facilities of the Hamilton HPC Service of Durham University.

Supplementary Material

Animated versions of Figure 3, showing the wave-propagation for 'Shot 2', with the P-wavefield and S-wavefield components separated.

References

Airoldi, G. M., Muirhead, J. D., Long, S. M., Zanella, E., & White, J. D. (2016). Flow dynamics in mid-Jurassic dikes and sills of the Ferrar large igneous province and implications for long-distance magma transport. Tectonophysics, 683, 182-199.

Archer, S.G., Bergman, S.C., Iliffe, J., Murphy, C.M. & Thornton, M. (2005) Palaeogene igneous rocks reveal new insights into the geodynamic evolution and petroleum potential of the Rockall Trough, NE Atlantic Margin. *Basin Res.*, **17**, 171–201. doi:10.1111/j.1365-2117.2005.00260.x

Bohlen, T. (2002) Parallel 3-D viscoelastic finite difference seismic modelling. *Comput. Geosci.*, **28**, 887–899.

Brocher, T.M. (2005) Empirical relations between elastic wavespeeds and density in the Earth's crust. *Bull. Seismol. Soc. Am.*, **95**, 2081–2092. doi:10.1785/0120050077

Cartwright, J. & Møller Hansen, D. (2006) Magma transport through the crust via interconnected sill complexes. *Geology*, **34(11)**, 929-932.

Deng, H.L. (1994) Acoustic-wave propagation in thin-layered media with steep reflectors. *Geophysics*, **59**, 1593–1604.

Dougherty, M.E. & Stephen, R.A. (1988) Seismic energy partitioning and scattering in laterally heterogeneous ocean crust. *Pure Appl. Geophys. PAGEOPH*, **128**, 195–229. doi:10.1007/BF01772597

Eide, C.H., Schofield, N., Lecomte, I., Buckley, S.J. & Howell, J.A. (2017) Seismic interpretation of sill complexes in sedimentary basins : implications for the sub-sill imaging problem. *J. Geol. Soc. London*, **175**, 193–209. doi:10.1144/jgs2017-096

Gallagher, J.W. & Dromgoole, P.W. (2007) Exploring below the basalt, offshore Faroes: a case history of sub-basalt imaging. *Pet. Geosci.*, **13**, 213–225. doi:10.1144/1354-079306-711

Goff, J.A., Holliger, K. & Levander, A.R. (1994) Modal fields: A new method for characterisation of random seismic velocity heterogeneity. *Geophys. Res. Lett.*, **21**, 493–496.

Goff, J.A. & Levander, A.R. (1996) Incorporating "sinuous connectivity" into stochastic models of crustal heterogeneity: Examples from the Lewisian gneiss complex, Scotland, the Franciscan formation, California, and the Hafafit Gneiss Complex, Egypt. *J. Geophys. Res. Solid Earth*, **101**, 8489–8501. doi:10.1029/96JB00110

Hardy, R.J., Bednar, J.B., Bednar, C., Fernandes, K. & Jones, S.M. (2008) Imaging Beneath Igneous Sills Using Reverse Time Depth Migration. *EAGE Expand. Abstr. 2008*.

Igel, H., 2017. *Computational seismology: a practical introduction*. Oxford University Press.

Jackson, C.A.L., Magee, C. & Jacquemyn, C. (2020) Rift-related magmatism influences petroleum systems development in the NE Irish Rockall Basin, offshore Ireland. *Pet. Geosci.*

Jones, I.F. (2013) Tutorial: The seismic response to strong vertical velocity change. *First Break*, **31**, 79–90. doi:10.3997/1365-2397.2013018

Larkin, S.P., Levander, A.R., Okaya, D. & Goff, J.A. (1996) A deterministic and stochastic velocity model for the Salton Trough/Basin and Range transition zone and constraints on magmatism during rifting. *J. Geophys. Res.*, **101**, 27883–27. doi:199610.1029/96JB02535

Lecomte, I., Lavadera, P.L., Botter, C., Anell, I., Buckley, S.J., Eide, C.H., Grippa, A., *et al.* (2016) 2(3)D convolution modelling of complex geological targets beyond – 1D convolution. *First Break*, **34**, 99–107. Retrieved from http://fb.eage.org/publication/content?id=84451

Levander, A.R., England, R.W., Smith, S.K., Hobbs, R.W., Goff, J.A. & Holliger, K. (1994) Stochastic characterization and seismic response of upper and middle crustal rocks based on the Lewisian gneiss complex, Scotland. *Geophys. J. Int.*, **119**, 243–259. doi:10.1111/j.1365-246X.1994.tb00925.x

Lomas, A. & Curtis, A. (2019) An introduction to Marchenko methods for imaging. *Geophysics*, **84**, F35–F45. doi:10.1190/geo2018-0068.1

Magee, C., Maharaj, S.M., Wrona, T. & Jackson, C.A.L. (2015) Controls on the expression of igneous intrusions in seismic reflection data. *Geosphere*, **11**, 1024–1041. doi:10.1130/GES01150.1

Magee, Craig, James D. Muirhead, Alex Karvelas, Simon P. Holford, Christopher AL Jackson,

Ian D. Bastow, Nick Schofield et al. "Lateral magma flow in mafic sill complexes." Geosphere 12, no. 3 (2016): 809-841.

Maresh, J., White, R.S., Hobbs, R.W. & Smallwood, J.R. (2006) Seismic attenuation of Atlantic margin basalts: Observations and modeling. *Geophysics*, **71**, B211–B221. doi:10.1190/1.2335875

Margrave, G.F. and Lamoureux, M.P., 2019. *Numerical methods of exploration seismology: With algorithms in MATLAB®*. Cambridge University Press.

Mark, N.J., Holford, S., Schofield, N., Eide, C.H., Pugliese, S., Watson, D. & Muirhead, D. (2019) Structural and lithological controls on the architecture of igneous intrusions: examples from the NW Australian Shelf. *Pet. Geosci.*

Mark, N.J., Schofield, N., Pugliese, S., Watson, D., Holford, S., Muirhead, D., Brown, R.J., *et al.* (2017) Igneous intrusions in the Faroe Shetland basin and their implications for hydrocarbon exploration; new insights from well and seismic data. *Mar. Pet. Geol.* doi:10.1016/j.marpetgeo.2017.12.005

Martini, F. & Bean, C.J. (2002) Interface scattering versus body scattering in subbasalt imaging and application of prestack wave equation datuming. *Geophysics*, **67**, 1593–1601. doi:10.1190/1.1512750

Morgan, J., Warner, M., Bell, R., Ashley, J., Barnes, D., Little, R., Roele, K., *et al.* (2013) Next-generation seismic experiments: Wide-angle, multi-azimuth, three-dimensional, full-waveform inversion. *Geophys. J. Int.*, **195**, 1657–1678. doi:10.1093/gji/ggt345

Muirhead, J.D., Airoldi, G., Rowland, J.V. and White, J.D. (2012) Interconnected sills and inclined sheet intrusions control shallow magma transport in the Ferrar large igneous province, Antarctica. *Bulletin*, *124*(1-2), pp.162-180.

Phillips, T. & Magee, C. (2020) Structural controls on the location, geometry, and longevity of an intraplate volcanic system - The Tuatara Volcanic Field, Great South Basin, New

Zealand. *J. Geol. Soc. London*. doi:10.31223/osf.io/b94ds

Rabbel, O., Galland, O., Mair, K., Lecomte, I., Senger, K., Spacapan, J.B. & Manceda, R. (2018) From field analogues to realistic seismic modelling : a case study of an oil-producing andesitic sill complex in the Neuquén Basin , Argentina.

Rateau, R., Schofield, N. & Smith. (2013) The potential role of igneous intrusions on hydrocarbon migration, West of Shetland. *Petroleum Geoscience, **19***(3), pp.259-272.

Schofield, N., Holford, S.P., Millett, J.M., Brown, D.J., Jolley, D., Passey, S.R., Muirhead, D., *et al.* (2015) Regional magma plumbing and emplacement mechanisms of the Faroe-Shetland Sill Complex: Implications for magma transport and petroleum systems within sedimentary basins. *Basin Res.*, 1–23.

Schofield, N.J., Brown, D.J., Magee, C. and Stevenson, C.T. (2012) Sill morphology and comparison of brittle and non-brittle emplacement mechanisms. *Journal of the Geological Society*, **169(2)**, 127-141.

Smallwood, J.R. & Maresh, J. (2002) The properties, morphology and distribution of igneous sills: modelling, borehole data and 3D seismic from the Faroe-Shetland area. *Geol. Soc. London, Spec. Publ.*, **197**, 271–306.

Stockwell, J.W. & Cohen, J.K. (2012) CWP/SU: Seismic Un*x Release No.43r3: an open source software package for seismic research and processing, Center for Wave Phenomena, Colorado School of Mines.

Thomson, K. & Hutton, D. (2004) Geometry and growth of sill complexes: insights using 3D seismic from the North Rockall Trough. *Bull. Volcanol.*, **66**, 364–375. doi:10.1007/s00445-003-0320-z

Walker, R., Stephens, T., Greenfield, C., Gill, S., Healy, D. and Poppe, S. (2020) Segment tip geometry of sheet intrusions, I: Theory and numerical models for the role of tip shape in controlling propagation pathways, *Volcanica, 4*(2),189-201.

Wessel, P. & Smith W. H. F. (1998) New, improved version of the Generic Mapping Tools released, EOS Trans. AGU, 79, 579.

Wright, T.J., Sigmundsson, F., Pagli, C., Belachew, M., Hamling, I.J., Brandsdóttir, B., Keir, D., Pedersen, R., Ayele, A., Ebinger, C. & Einarsson, P. (2012) Geophysical constraints on the dynamics of spreading centres from rifting episodes on land., *Nature Geoscience,* 5(4)

Zanoth, S.R., Saenger, E.H., Kruger, O.S. & Shapiro, S.A. (2007) Leaky mode: A mechanism of horizontal seismic attenuation in a gas-hydrate-bearing sediment. *Geophysics*, **72**, E159. doi:10.1190/1.2750375

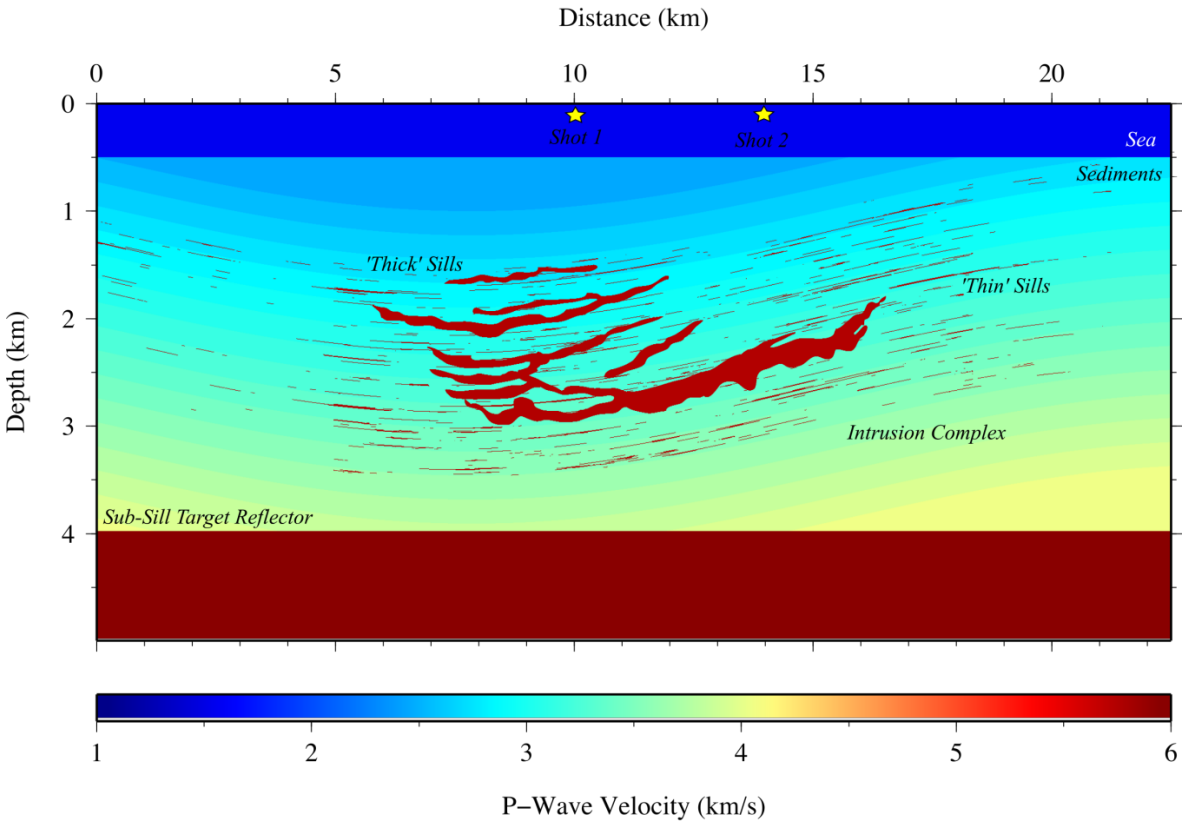

Figure 1: P-wave velocity model containing both seismically resolvable 'thick' sills taken from the interpreted seismic data, and unresolvable 'thin' sills. Two shot locations are presented here, 'Shot 1' at 10 km and 'Shot 2' at 14 km.

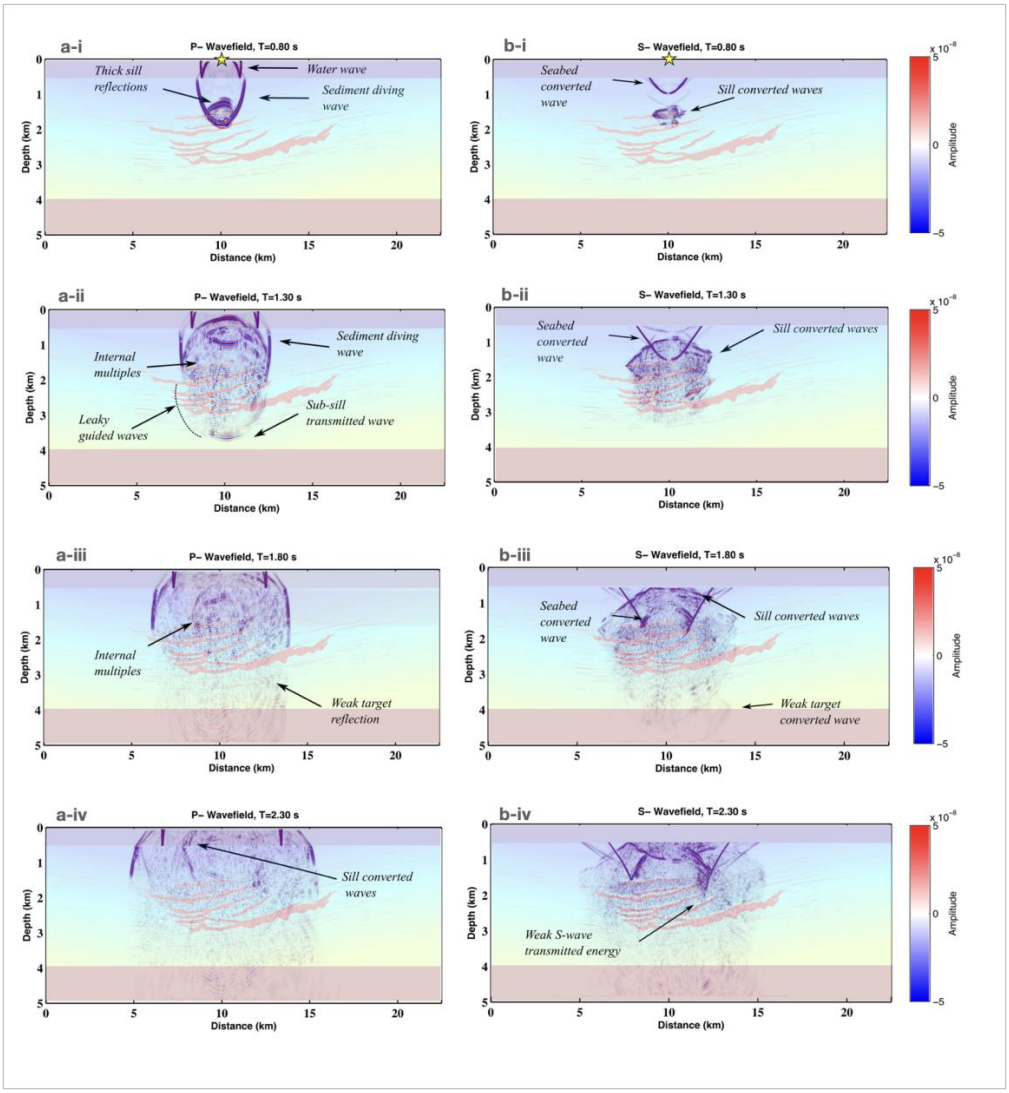

Figure 2: Snapshots of seismic wave propagation from 'Shot 1' (yellow star), showing the separated P-wavefield (a) and S-wavefield (b) after 0.80 (i), 1.30 (ii), 1.80 (iii) and 2.30 (iv) seconds.

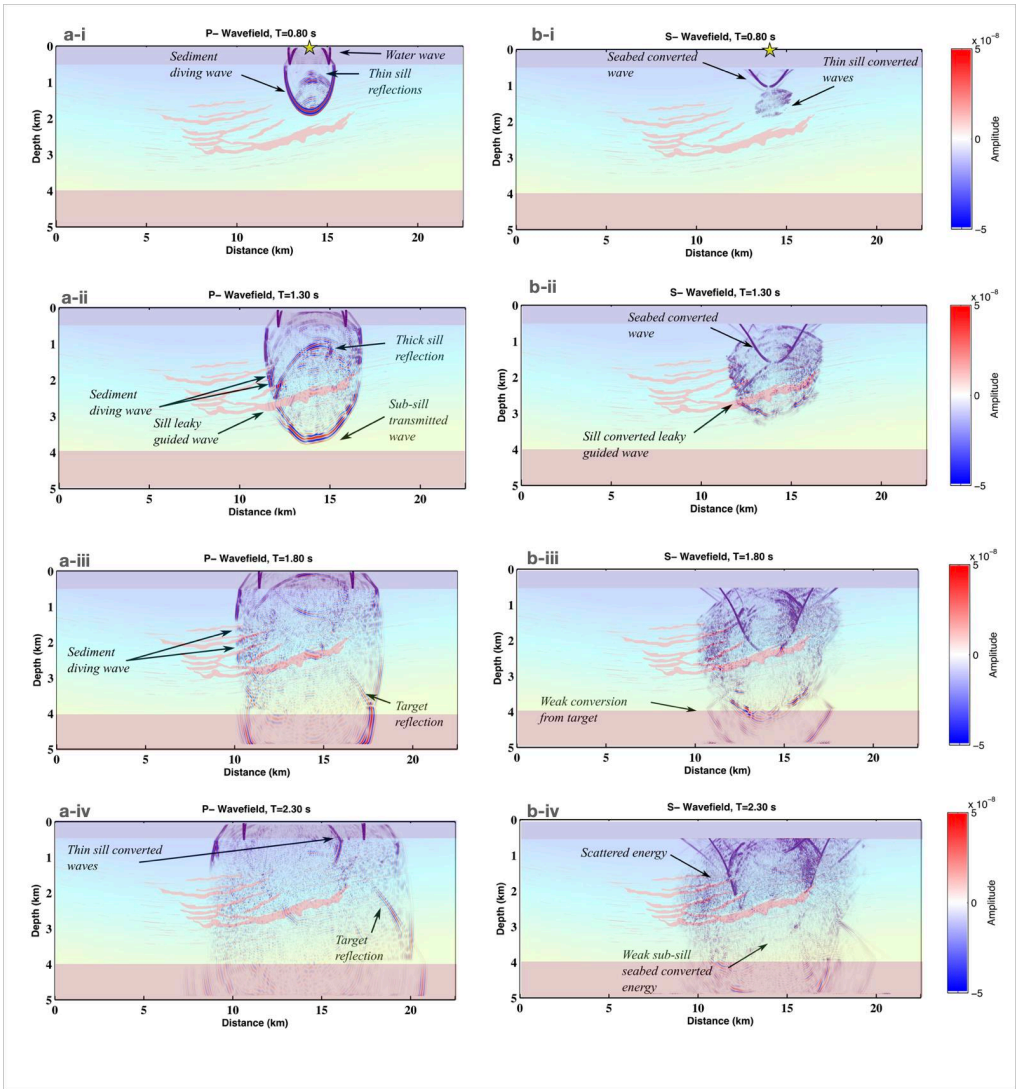

Figure 3: Snapshots of seismic wave propagation from 'Shot 2 (yellow star), showing the separated P-wavefield (a) and S-wavefield (b) after 0.80 (i), 1.30 (ii), 1.80 (iii) and 2.30 (iv) seconds..

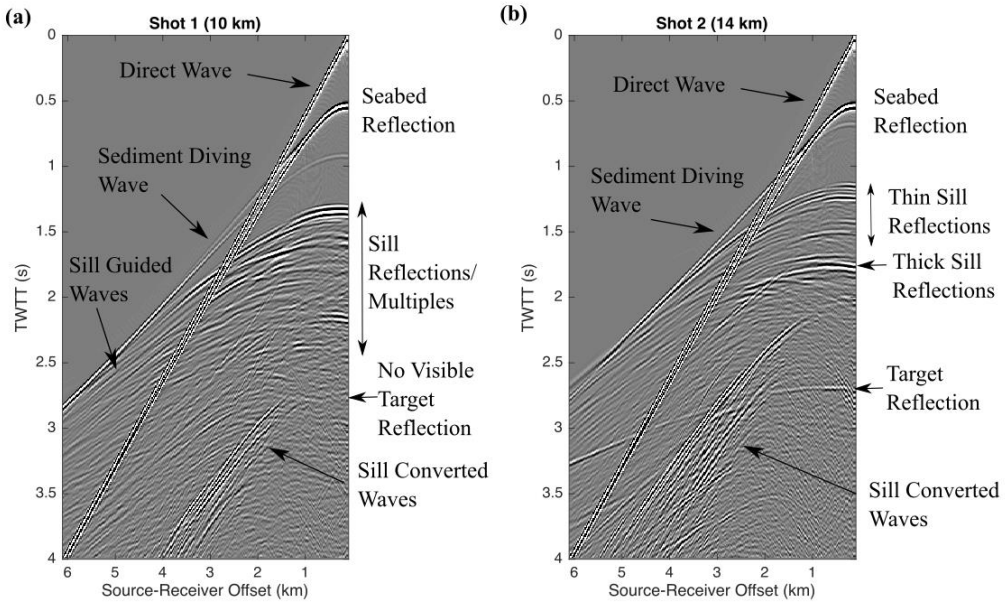

Figure 4: Simulated shot gathers for (a) Shot 1 at 10 km and (b) Shot 2 at 14 km, with the main observed arrivals labelled.

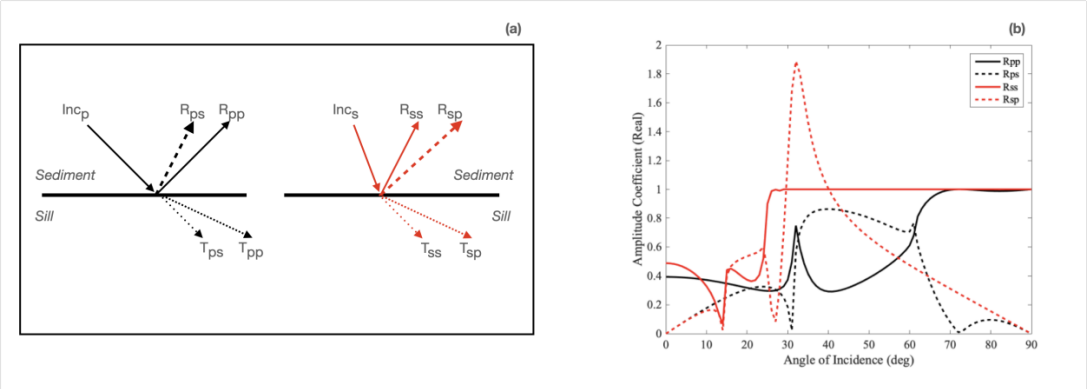

Figure 5: (a) Schematic of the transmitted and reflected phase conversions that occur at a sediment-sill boundary , from an incident P-wave (left) and S-wave (right) (b) Zoeppritz plane wave reflection coefficients for an incident P-wave (black) and S-wave (red) at a sediment/intrusion boundary (assumed to be a half space), plotted against the angle of incidence. Sediment: V_p=3 km/s, V_s=1.4 km/s, rho=2.2 kg/m^3. Intrusion: V_p=5.75 km/s, V_s=3.4 km/s, rho=2.7 kg/m^3. Rpp = reflected P-wave, Rss = reflected S-wave. Reflected converted phases (Rps = P-wave to S-wave, Rsp = S-wave to P-wave) are shown by dashed lines. Transmission coefficients are not shown here.